Crystal Orientation Change and Its Origin in One-Dimensional Nanoconfinement Constructed by Polystyrene-*block*-poly(ethylene oxide) Single Crystal Mats

Ming-Siao Hsiao,[†] Joseph X. Zheng,[†] Siwei Leng,[†] Ryan M. Van Horn,[†] Roderic P. Quirk,[†] Edwin L. Thomas,[‡] Hsin-Lung Chen,[§] Benjamin S. Hsiao,[||] Lixia Rong,[||] Bernard Lotz,[⊥] and Stephen Z. D. Cheng*[,†]

Maurice Morton Institute and Department of Polymer Science, The University of Akron, Akron, Ohio 44325-3909; Department of Materials Science and Engineering, Massachusetts Institute of Technology, Cambridge, Massachusetts 02139; Department of Chemical Engineering, National Tsing-Hua University, Hsinchu, Taiwan, 300, ROC; Department of Chemistry, The State University of New York at Stony Brook, Stony Brook, New York 11794-3400; and Institut Charles Sadron, 23, Rue du Loess, Strasbourg 67034, France

Received July 21, 2008; Revised Manuscript Received September 4, 2008

ABSTRACT: Utilizing crystalline−amorphous block copolymers, such as in the case of polystyrene-*block*-poly(ethylene oxide) (PS-*b*-PEO), under a large amplitude shear process provides an opportunity for investigating crystal growth and orientation within nanoconfinements at different supercoolings. However, the internal stress generated during the shearing process and the structural defects embedded in the phase-separated morphology inevitably play roles in affecting the confinement effect on the crystallization of the crystalline blocks. In this study, we designed a one-dimensional (1D), defect-free confinement constructed by PS-*b*-PEO single crystal mats collected in dilute solution. Each single crystal possessed a square-shaped, "sandwiched" lamellar structure, and it consisted of a PEO single crystal layer between two PS nanolayers formed by the tethered PS blocks on the PEO single crystal top and bottom fold surfaces. Furthermore, in these single crystal mats the glass transition temperature of the PS blocks is higher than the melting temperature of the PEO single crystals. We melted the PEO crystals between the two vitrified PS nanolayers, and the PEO blocks were recrystallized isothermally by quenching the mats to preset recrystallization temperatures (T_{rx}). The orientation change of the PEO crystals with respect to the "sandwiched" lamellar normal at different T_{rx} values was investigated via 2D small-angle and wide-angle X-ray scattering experiments. It was observed that the PEO *c*-axis orientation underwent a sharp change from homogeneous (perpendicular to the lamellar normal) in the low T_{rx} region to approximately homeotropic (parallel to the lamellar normal) in the high T_{rx} region. The results showed that this change of the PEO crystal orientation takes place within a few degrees Celsius. Microscopically, the crystal orientation might be determined from the status of critical nuclei formation due to the size and shape of this 1D confinement. This likely included a competition between the high tethering density (the junctions) of the PEO blocks at the PS interfaces leading to the homeotropic orientation with an anisotropic conformational orientation of the PEO blocks in the melt and the anisotropic density fluctuations within the 1D confined layer which could lead to an anisotropic ability for the PEO blocks to overcome the nucleation barrier to form the homogeneous orientation. The resolution of these two factors might explain the origin of the crystal orientation change in 1D confined crystallization. Analysis of the apparent crystallite size in these mats along both the orthogonally oriented [120] directions of the PEO crystals after recrystallization indicated that a change in the PEO crystal growth dimension from 1D to 2D occurs within this narrow T_{rx} region corresponding to the location of the crystal orientation change.

Introduction

In the past 20 years, attention has been paid to polymer crystallization behavior in nanoconfined geometries using microphase separation of crystalline−amorphous diblock copolymers as templates. By varying the volume fractions of those diblock copolymers, different phase structures, such as lamellae, cylinders, and spheres, can be generated. The three main phase transitions during cooling of those copolymers involve an order−disorder transition identified by an order−disorder transition temperature (T_{ODT}), a vitrification of the amorphous blocks represented by a glass transition temperature (T_g), and a solidification process of the crystalline blocks identified by a crystal melting temperature (T_m). For upper critical solution temperature systems, when the sequence of these three phase transitions is in the following order—the T_{ODT} of the diblock copolymer is the highest, followed by the vitrification of the amorphous block to form the glassy matrix and, finally, the crystallization of the crystalline blocks takes place at the lowest temperature (T_x)—a specifically tailored, nanoconfined crystallization can be achieved.[1−33]

Crystallization kinetics and crystal orientation changes with respect to the lamellar normal are two issues that have been addressed in confined crystallization utilizing lamellar diblock copolymers. In order to investigate polymer crystallization within the one-dimensional (1D) nanoconfinements constructed by the crystalline−amorphous diblock copolymers with symmetric volume compositions of the blocks, a large sample size (on the order of millimeters) with uniformly oriented, alternating lamellar phase structure is required for conducting wide- and small-angle X-ray scattering (WAXS and SAXS) experiments. Using large amplitude mechanical shear force on the sample is a traditional technique to achieve highly oriented samples. In almost all cases, however, the perfectly alternating lamellar

* To whom correspondence should be addressed. E-mail: scheng@uakron.edu.
[†] The University of Akron.
[‡] Massachusetts Institute of Technology.
[§] National Tsing-Hua University.
[||] The State University of New York at Stony Brook.
[⊥] Institut Charles Sadron.

10.1021/ma801641w CCC: $40.75
Published on Web 10/10/2008

phase structure is not achieved due to the existence of phase structure defects such as edge and screw dislocations and grains and subgrain boundaries.[34−36] These defects inevitably release the confinement and drastically affect the crystallization kinetics.[37,60] Despite these problems, the chain orientation changes of poly(ethylene oxide) crystals in 1D and 2D confined environments were systematically investigated in the past several years through a series of diblock copolymers of polystyrene-*block*-poly(ethylene oxide) (PS-*b*-PEO) with different molecular weights and compositions.[18−22,28,30,32] It was concluded that crystal orientation can be tailored by the control of T_x[18] and the confinement size[28] as well as the initial stage of crystal growth.[19]

In a previous publication, we have presented a new approach for the study of PEO crystallization in 1D, defect-free confinement utilizing PS-*b*-PEO single crystals grown in dilute solution as a template.[38] In this case, the "sandwiched" lamellar templates were formed with a PEO single crystal in the middle and two PS nanolayers covering both sides of the PEO single crystal basal surfaces. This type of sample preparation eliminates phase structure defects that generate interconnections between lamellae in the 1D confinement. When two thin PS nanolayers possess a T_g^{PS} which is higher than the T_m^{PEO} of PEO single crystals, the samples can be heated to melt the PEO single crystals without damage to the lamellar structural integrity. The PEO blocks will thus undergo a recrystallization process under a 1D confinement generated by the two PS nanolayers after the PEO blocks are quenched to a preset recrystallization temperature (T_{rx}). We can then utilize the electron diffraction (ED) technique in transmission electron microscopy (TEM) to study microscopic crystal orientation in one single crystal of PS-*b*-PEO after recrystallization. Compared with the PEO crystallization in sheared lamellar PS-*b*-PEO samples, the PEO recrystallization in this "sandwiched" lamellar single crystal exhibits significant differences in both crystallization behavior and crystal orientation.[37] First, the PEO blocks do not recrystallize at $T_{rx} > -5$ °C, indicating the absence of heterogeneous nucleation in the PEO blocks of the PS-*b*-PEO single crystals. Second, crystallographic analyses based on the ED results obtained from the recrystallized PEO block crystals show three different *c*-axis orientations (random orientation, parallel to the lamellar normal, and inclined 26° with respect to the lamellar normal) depending upon T_{rx} values.

Although the ED technique possesses advantages for precisely determining the crystal orientation, this technique has also a limitation in analyzing the full 3D space of the sample's crystallography. Since the maximum tilting stage angle in TEM ED experiments is 60°, it is impossible to position the electron beam along the edge direction of the "sandwiched" lamella. Yet, the diffraction patterns obtained along the edge direction are essential for the analysis of the crystal orientation changes at different T_{rx} values.

Despite all the investigations reported concerning crystal orientation in nanoconfined crystallization, important issues still remain: Is the crystal orientation change a general observation in nanoconfined crystallization of semicrystalline diblock polymers? If so, what is the mechanism for this crystal orientation change? For this purpose, we have extended the single crystal approach to forming single crystal mats by stacking the PS-*b*-PEO single crystals together. The single crystal mats thus do not contain any phase structure defects. Namely, each of the PEO layers is completely isolated by the PS thin layers in the mats. Using these stacked, "sandwiched" single crystal mats as templates, we can utilize WAXS and SAXS experiments to investigate detailed PEO crystal orientation changes with respect to T_{rx} by taking 2D diffraction patterns from both the lamellar normal and the edge directions of these single crystal mats.

Table 1. Molecular Weight and T_{ODT} Values of a Series of PS-*b*-PEO Samples

PS-*b*-PEO	M_n^{PS} (g/mol)	M_n^{PEO} (g/mol)	f_{PEO}	T_{ODT}[a] (°C)
61K-*b*-57K	61 300	57 000	0.468	>200
65K-*b*-35K	65 000	35 000	0.335	>200
26K-*b*-23K	26 100	23 100	0.456	190

[a] The T_{ODT} were measured from temperature dependence 1D SAXS curves of a series of PS-*b*-PEO diblock copolymers.

Experimental Section

Materials and Sample Preparation. Three PS-*b*-PEO diblock copolymers having M_n^{PS} = 61K g/mol and M_n^{PEO} = 57K g/mol, M_n^{PS} = 65K g/mol and M_n^{PEO} = 35K g/mol, and M_n^{PS} = 26K g/mol and M_n^{PEO} = 23K g/mol were used in this study. The detailed sequential living anionic polymerization of the samples was described previously.[39] Briefly speaking, the M_n^{PS} precursors were first synthesized, and their polydispersities were characterized by size exclusion chromatography (SEC) using polystyrene standards. The M_n^{PEO} values were determined by proton nuclear magnetic resonance (^{1}H NMR) spectroscopy. The polydispersities of the final diblock copolymers were determined by SEC using the universal calibration. The PEO crystal density (ρ_{PEO}^c) is 1.239 g/cm^3, and the amorphous PEO bulk density (ρ_{PEO}^a) is 1.124 g/cm^3. The PS bulk amorphous density (ρ_{PS}^a) is 1.052 g/cm^3.[34] The molecular weights, volume fraction of PEO blocks, and the T_{ODT} of the melt of these three samples are listed in Table 1.

The single crystal preparation of PEO-*b*-PS diblock copolymers has been described in the literature.[40−43] Growing a large amount of uniform, large size PS-*b*-PEO single crystals was a prerequisite for preparing single crystal mats. In this study, single crystals of PS-*b*-PEO were grown in a mixed solution of chlorobenzene and octane with a 1:1 weight ratio and a concentration of 0.05 wt % after the solution was filtered with PTFE molecular sieves with a diameter of 0.45 μm. Solvents used here were HPLC grade, dried with CaH_2, and freshly distilled. The polymer samples were dissolved above T_d = 42 °C in a temperature-controlled oil bath. The self-seeding procedure was utilized to achieve a number of single crystals with a uniform size.[40,44] The procedure is briefly described here. The homogeneous polymer solution was crystallized at room temperature and reheated to a seeding temperature 1 °C lower than the T_d and kept there for 20 min. The sample was then quickly quenched to a preset crystallization temperature (T_x) in an isothermal oil bath to grow single crystals.[38,40−44] Note that only a lamellar phase structure was formed in the solution of these three PS-*b*-PEO samples disregarding their volume compositions and phase structures formed in the condensed state.

Single crystal suspensions in the solution were filtered following the published procedure to remove uncrystallized PS-*b*-PEO polymers.[45,46] The filtered single crystals were then washed twice with the mixed solvent before the solution was quenched into large excess ethylbenzene.[40,44] Note that ethylbenzene is a poor solvent for both PS and PEO blocks and that the PS blocks are easily vitrified during quenching and precipitation of the single crystals. The PS-*b*-PEO single crystals were then gently precipitated and carefully collected at the bottom of the test tubes and dried in vacuum at room temperature for 3 days to obtain the single crystal mats.

^{1}H NMR and SEC experiments were performed on the mat samples prepared by redissolving the single crystals in the appropriate solvent. No changes in molecular weights, molecular weight distributions, and PEO composition were observed, suggesting that there was no molecular fractionation during the PEO block crystallization in dilute solution.

Equipment and Experiments. PS-*b*-PEO single crystal images were obtained on an Olympus BH-2 phase contrast optical microscope (PCOM). The scale bar was calibrated in both lateral and vertical directions using the standard grid.

In order to determine the T_m^{PEO} of the PEO layer and the T_g^{PS} of the PS layer in PS-*b*-PEO single crystal mats, Perkin-Elmer PYRIS diamond differential scanning calorimetry (DSC) coupled with an

Intracooler 2P apparatus was used. A typical sample weight of the single crystal mats was 0.1 mg, and the heating rate was at 10 °C/min. The endothermic peak temperature was assigned to be the T_m^{PEO}, and the weight percent crystallinity was calculated based on the equilibrium heat of fusion for PEO crystals reported (8.66 kJ/mol).[47] For this calculation, the PEO weight fraction in the PS-*b*-PEO samples was normalized. The T_g^{PS} was identified in the DSC measurements as the midpoint of the stepwise increase of the heat capacity. In order to study the recrystallization event of PEO blocks between two glassy layers, the single crystal mats were also cooled at a 10 °C/min in the DSC experiments after complete melting of the PEO single crystals. Subsequent heating experiments were also recorded at the same rate.

Simultaneous 2D SAXS and WAXS experiments were conducted at the synchrotron X-ray beamline X27C at the National Synchrotron Light Source at the Brookhaven National Laboratory. The wavelength of the X-ray beam was 0.1366 nm. The zero pixel of the 2D SAXS patterns was calibrated using silver behenate with the first-order scattering vector q ($q = 4\pi \sin\theta/\lambda$, where λ is the wavelength and 2θ is the scattering angle and $q = 1.076$ nm^{-1}). 2D WAXS patterns were calibrated using α-Al_2O_3 with known crystal diffraction at $2\theta = 28.47°$.

To confirm the T_g^{PS} measured in DSC, the devitrification process of the glassy PS thin layers in the PS-*b*-PEO single crystal was studied by monitoring the change in *d*-spacing of the single crystal mats during heating via a SAXS experiment equipped with a hot stage. This type of SAXS measurement was carried out using a Bruker Nanostar SAXS instrument. The X-ray source was a 1.5 kW X-ray generator (Kristalloflex 760) equipped with a Cu tube (operated at 35 mA and 40 kV). The scattering intensities and patterns were detected by a 2D position-sensitive detector (Bruker AXS) with 512 × 512 channels. The area scattering patterns of the anisotropic samples have been geometrically averaged to generate the intensity profile's output as plots of the scattering intensity versus the scattering vector, q. The scattering intensities have been corrected by the empty beam scattering and the sensitivity of each pixel of the area detector.

2D WAXS experiments were also conducted using an imaging system (Rigaku, R-AXIS-IV) with an 18 kW rotating anode X-ray generator. The received patterns were calibrated via the same procedure as in the synchrotron X-ray experiments. A 2 h exposure time was adequate for obtaining a high-quality pattern. In all 2D X-ray experiments, background scattering was subtracted from the sample scans.

In order to analyze the apparent crystallite sizes along the normal direction of the (120) plane (the [4$\bar{2}$1] direction) of the PEO crystals in the 1D confined environment, the Scherrer equation was used in the form of

$$D_{120} = \frac{K\lambda}{\beta_{120}\cos\theta} \quad (1)$$

where D_{120} is the apparent crystallite size along the [4$\bar{2}$1] direction, K is the shape factor, or the Scherrer constant (a value of 0.94 is used in this case), β_{120} is the line breadth, and θ is the half-scattering angle. In most cases, β_{120} is taken to be the half-width at half-maximum (hwhm) of a (120) diffraction. Assuming that the diffraction peak shape obeyed a Gaussian function, Warren's correction can be used to correct instrument broadening:[48]

$$\frac{\beta_{120}}{B_{120}} = \sqrt{1 - \frac{b^2}{B_{120}^2}} \quad (2)$$

where B_{120} is the experimentally observed hwhm of the diffraction peak and b is the hwhm of a standard specimen diffraction. To ensure a good calibration, the apparent crystallite size of the standard specimen should be >60 nm. A quartz line at 60.0° was taken for the standard b.

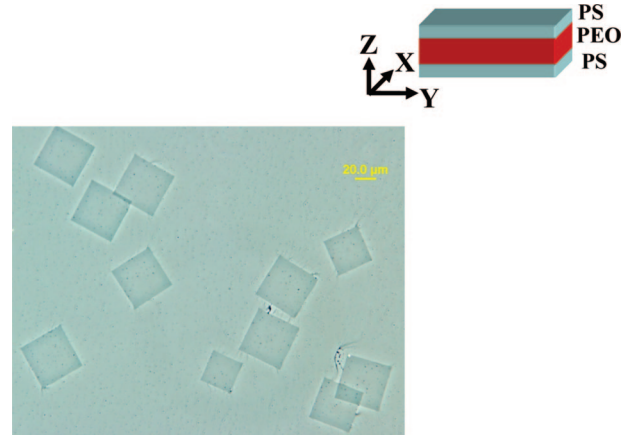

Figure 1. Phase contrast optical microscopy image of PS-*b*-PEO diblock copolymer single crystals (65K-*b*-35K) (a) and the sandwiched lamellar structure illustrated by a schematic drawing (b).

Results and Discussion

Structure Parameters and Thermodynamic Properties of PS-*b*-PEO Single Crystal Mats. Figure 1 shows a PCOM image that illustrates the uniform, square single crystals of PS-*b*-PEO diblock copolymer (65K-*b*-35K) grown in chlorobenzene/octane mixed solvent at $T_x = 30$ °C. These crystals are bound by four (120) crystallographic planes. The sizes of the PS-*b*-PEO single crystals are identical due to the self-seeding procedure, and their lateral dimensions exceed 40 μm. As reported in the previous publications,[40−43] glassy PS blocks completely cover both the top and bottom basal surfaces of the single crystals. Therefore, a "sandwiched" lamellar structure is obtained, as schematically illustrated in Figure 1. Note that in the PS-*b*-PEO single crystals the ratio between the lateral dimension and the single crystal thickness is over 4000.

Based on the AFM observations and calculations (the detailed procedure was reported previously[42,43]), the thicknesses of the PEO single crystal layer and glassy PS layer of these three PS-*b*-PEO samples at $T_x = 30$ °C are listed in Table 2. For example, the thickness of the PEO single crystal is $d_{PEO} = 10.1$ nm, and the thickness of the PS layer is $d_{PS} = 11.0$ nm for PS-*b*-PEO (65K-*b*-35K). The d_{PEO} represents the confined size. The thicknesses of d_{PS} and d_{PEO} of the other two block copolymers are also listed in this table. It is evident that the confined sizes for PEO block recrystallization in these three copolymers are similar in a narrow range between 10 and 12 nm. In Table 2, the tethering densities of PEO blocks (σ) on the PS glassy substrates are also calculated and included. These σ values range from 0.08 to 0.17 nm^{-2}, and their corresponding reduced tethering densities ($\tilde{\sigma}$) are between 17.3 and 21.0 as listed in Table 2. Furthermore, it should be noted that by changing the T_x values, the reduced tethering density can be varied due to the change in the d_{PEO} value with supercooling.[41]

In order to make sure that the PS layers are still in the glassy state when the PEO single crystals have been melted, the T_m^{PEO} values of the PEO single crystals and T_g^{PS} values of the PS layers are measured via DSC experiments for the PS-*b*-PEO single crystal mats. For example, PS-*b*-PEO (26K-*b*-23K) single crystal mats crystallized at $T_x = 30$ °C in the mixed dilute solution show a sharp endothermic peak with a T_m^{PEO} of 58.0 ° C, as shown in Figure 2. Using the heat of fusion measured in Figure 2, the calculated crystallinity is ~95%. The heat capacity increase at the T_g^{PS} can also be seen in this DSC thermal diagram, and it is included in Figure 2 as an inset. This inset has been multiplied 10 times in order to clearly illustrate the T_g^{PS}. It must be mentioned that the heat capacity increase at the T_g^{PS}, ΔC_p, of these block copolymers are weaker and their

Table 2. Layer Thickness and Thermal Properties for a Series of PEO-*b*-PS Single Crystal Mats[a]

PS-*b*-PEO	L (nm)	d_{PEO} (nm)	d_{PS} (nm)	T_m^{PEO} (°C)	T_g^{PS} (mats) (°C)	T_g^{PS} (bulk) (°C)[a]	σ (nm^{-2})	$\tilde{\sigma}$
61.3K-*b*-57K	27.6	12.2	7.7	59.5	85 (a, b)	97.0	0.08	21.0
65K-*b*-35K	32.1	10.1	11.0	60.0	>90 (b), 85−90 (a, c)	97.4	0.11	17.3
26K-*b*-23K	25.9	11.9	7.0	58.0	65 (a, b)	79.0	0.17	18.2

[a] The T_m^{PEO} and T_g^{PS} were measured in (a) DSC, (b) temperature-dependent 2D SAXS, and (c) AFM equipped with hot stage.

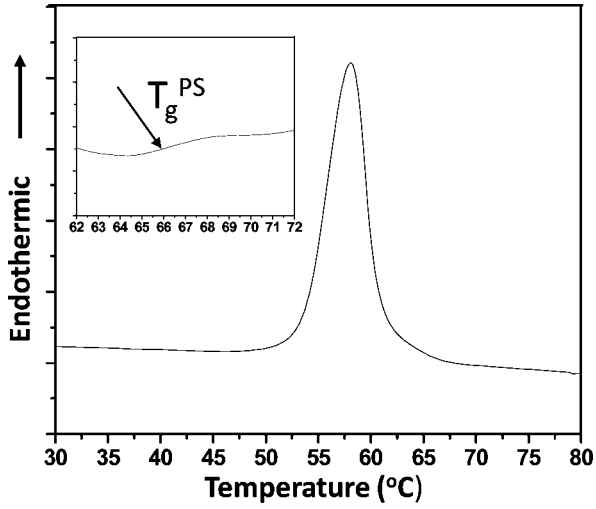

Figure 2. DSC melting thermal diagram for PS-*b*-PEO single crystals mats (26K-*b*-23K). The inset represents the glass transition region of the mats with an enlarged heat flow scale (×10).

transition widths are broader compared with a normal heat capacity increase for PS homopolymer.[37] The T_g^{PS} values of these three diblock copolymer samples are listed in Table 2. Note that the glass transition is a region rather than a single temperature. The beginning of the T_g^{PS} should be the upper-limit temperature to which the mat samples can be heated without disordering the sandwiched lamellae.

The real test of this upper-limit temperature of the vitrified PS thin layer in the mats is achieved by using the temperature-dependent 2D SAXS. We know that the "sandwiched" single crystals in the mats exhibit a lamellar structure. However, this lamellar structure as grown in solution is governed by the single crystal growth, and this structure is different from the equilibrium microphase-separated structure in the bulk. For the diblock copolymers having close to symmetric volume fractions, such as PS-*b*-PEO (26K-*b*-23K) and (61K-*b*-57K), they will also form the lamellar structure in the bulk but with different layer spacing. For PS-*b*-PEO (65K-*b*-35K), its equilibrium phase structure is hexagonal cylinders. When the temperature is increased above the T_g^{PS}, these PS-*b*-PEO single crystal mats should relax to their equilibrium phase structure, and this relaxation will be reflected in the sudden change of the SAXS patterns. Therefore, the lamellar single crystals in the mats are thermodynamically metastable or unstable compared with the phase-separated structure in the bulk.[49]

Figures 3a−d show a set of 2D SAXS patterns for PS-*b*-PEO (26K-*b*-23K) single crystal mats along the direction perpendicular to the lamellar normal (the *xy*-plane as shown in the schematic of Figure 1) during heating to different temperatures. The azimuthal integrations of these 2D SAXS patterns generate 1D SAXS diagrams as shown in Figure 3e. It is evident that up to 5 orders of diffraction peaks can be clearly identified, and the layer spacing of this lamellar structure is 25.6 nm. These results indicate that in this mat sample the stacking of these sandwiched lamellae possesses a long-range, 1D layer orientational order. The lamellar thickness deduced in this SAXS data is nearly identical to the measurements obtained using the AFM technique (25.6 nm vs 25.9 nm). Figure 3f shows the relationship between the layer spacing values and temperatures. Upon increase of the temperature, the measured layer spacing exhibits a sudden increase from 25.6 to 31.9 nm at 65 °C, indicating that the PS blocks can no long hold the thin PS layers in their vitrified state and that the PS-*b*-PEO copolymer is returning to the equilibrium heterogeneous melt with a larger layer spacing. This temperature of 65 °C is thus recognized precisely as the upper-limit temperature for the PEO-*b*-PS (26K-*b*-23K) single crystal mats. The upper-limit temperatures of the other two diblock copolymer single crystal mats are also listed in Table 2.

An interesting observation is that the values of T_g^{PS} in these three PS-*b*-PEO mats are not only much lower than those in PS homopolymer with equal molecular weights, but also lower than their corresponding values measured in their corresponding bulk PS-*b*-PEO, as listed in Table 2. This difference in T_g^{PS} between the mats and the bulk PS-*b*-PEO might be related to the difference in PS layer thickness. This reduction in T_g^{PS} of the PS layers has also been observed in different types of thin PS films, such as free-standing films and thin PS layers supported by a substrate.[50−52] Furthermore, high reduced tethering densities in these mats cause distortion of the PS chain conformation and may also lead to internal stresses which decrease the T_g^{PS} values.[53−55]

As listed in Table 2, the T_m^{PEO} of PS-*b*-PEO (26K-*b*-23K) single crystal mats is 7 °C lower than the upper-limit temperatures of the glassy PS nanolayers. This serves as a window within which the mats can be heated to melt the PEO single crystals and retain the vitrified PS nanolayers. The PEO blocks can then be recrystallized by quenching the samples to preset T_{rx} values. The other two diblock copolymer mats have even broader windows compared with PS-*b*-PEO (26K-*b*-23K) due to the fact that PS blocks possess higher molecular weights as well as larger thicknesses in the PS nanolayers, as shown in Table 2. Therefore, these single crystals mats can be templates for investigating the recrystallization behavior of the PEO blocks in 1D confinement without phase structure defects.

In order to prove that we can practically use this window to carry out the recrystallization of the PEO blocks, we have also conducted a DSC experiment by heating the PS-*b*-PEO (26K-*b*-23K) single crystal mat sample to 64 °C, which is 1 °C lower than the T_g^{PS} observed, and held it there for 5 min. The sample was then cooled to −40 °C at a cooling rate of 10 °C/min. An exothermic peak observed at −7 °C as shown in Figure 4a. This value is substantially lower than those observed in mechanically sheared lamellar diblock copolymer samples. For example, the PEO blocks crystallized at 27 °C in a bulk lamellar confinement of a PS-*b*-PEO system via mechanical shearing as determined by DSC during cooling.[37] The subsequent heating process results in a broad endothermic peak around 53 °C, as shown in Figure 4b. The comparison of this lower and broader melting thermal diagram with that in Figure 2 indicates that the recrystallized PEO crystals melt at much lower temperatures (note the starting temperature of the melting is slightly above 30 °C and leads to a broad endothermic peak due to continuous crystal annealing[49]). Therefore, the crystals formed during the recrystallization while cooling, similar to the case in single crystals of PS-*b*-PEO,[38] are caused by homogeneous nucleation that is both smaller in size and farther away from the equilibrium.[49,56]

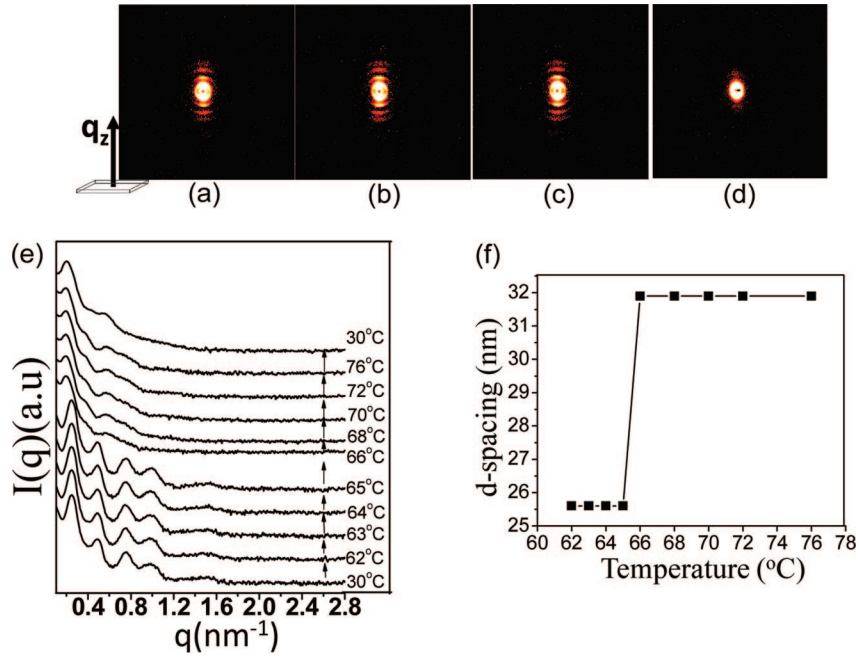

Figure 3. Set of 2D SAXS patterns (T = 60, 63, 65, and 66 °C, from left to right) taken from PS-*b*-PEO single crystals mats (26K-*b*-23K) by aligning the X-ray beam along the *xy*-plane (a−d) and its 1D SAXS curves after azimuthal integrations (e). A relationship of temperature and layer spacing shows a sudden change of the layer spacing at 65 °C (f).

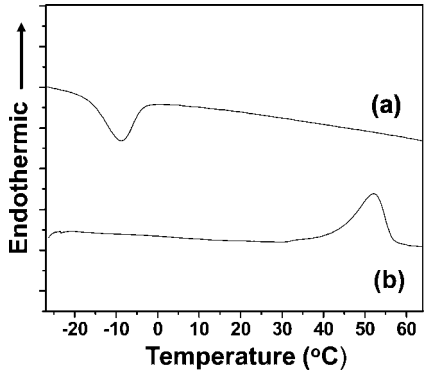

Figure 4. DSC cooling thermal diagram for PS-*b*-PEO single crystals mats (26K-*b*-23K) after holding at 64 °C for 5 min. The exothermic peak appears at −7 °C, indicating that crystallization of the PEO blocks occurs at much lower temperature compared with that of the mechanically sheared PS-*b*-PEO samples (a). The subsequent heating experiment in DSC shows a broader and lower melting endothermic event starting at slightly above 30 °C compared with that in Figure 2b.

PEO Crystal Orientation Dependence on T_{rx}. The PEO crystal orientation in PS-*b*-PEO single crystal mats can be examined via simultaneous 2D WAXS and SAXS techniques. When three different PS-*b*-PEO single crystal mats were heated and held for 5 min at 64 °C for PS-*b*-PEO (26K-*b*-23K) and (65K-*b*-35K) and 67 °C for PS-*b*-PEO (61.3K-*b*-57K), the PEO single crystals were completely melted between the two vitrified PS layers. These mats were quickly quenched into liquid nitrogen for 10 min and then brought back to room temperature for X-ray measurements. Figures 5a,c show two 2D SAXS patterns of PS-*b*-PEO (65K-*b*-35K) when the X-ray beam was directed along the *xy*-plane (perpendicular to the lamellar normal) and the *z*-direction (see the schematic of Figure 1). The 2D SAXS pattern along the *z*-direction (Figure 5c) only exhibits minimal scattering. However, in the pattern along the *xy*-plane as shown in Figure 5a, the long-range lamellar diffractions can be found with higher order diffractions, indicating that the layer structure in the mat is retained.

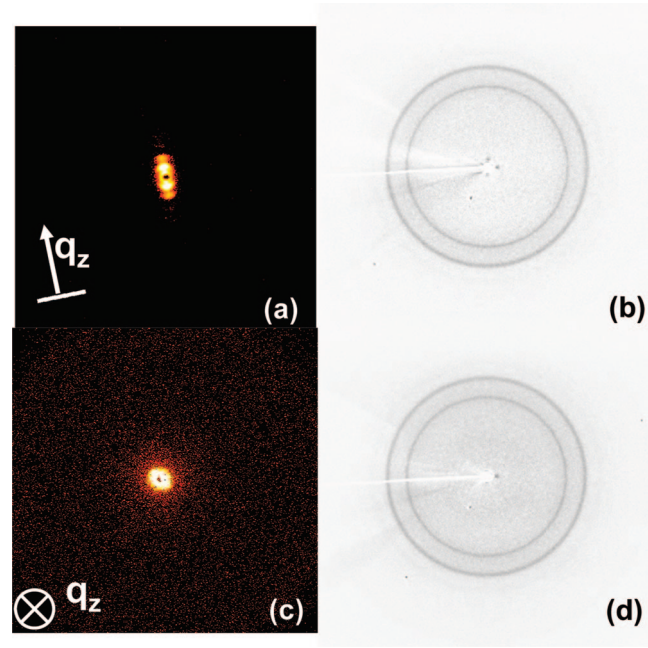

Figure 5. Set of 2D WAXS patterns of the PS-*b*-PEO single crystal mats (65K-*b*-35K) quenched to liquid N_2 for 10 min after staying at 64 °C for 5 min when the X-ray is along the *xy*-plane (a) and along the *z*-direction (b).

The results of 2D WAXS patterns in Figures 5b,d obtained along both the *xy*-plane and the *z*-direction are identical and exhibit two major isotropic diffraction rings with *d*-spacings of 0.46 and 0.39 nm. The inner ring with a *d*-spacing of 0.46 nm is indexed as (120), while the outside ring consists of overlapped ($\bar{1}$32), (032), (112), ($\bar{2}$12), ($\bar{1}$24), ($\bar{2}$04), and (004) diffractions with a *d*-spacing of 0.39 nm. These isotropic ring patterns indicate that a random PEO crystal orientation exists within this 1D defect-free confinement. This observation is identical to the results found in mechanically sheared PS-*b*-PEO lamellae in the bulk.[18,28] During quenching into liquid N_2, a large number of homogeneous nuclei are created. The primary nucleation

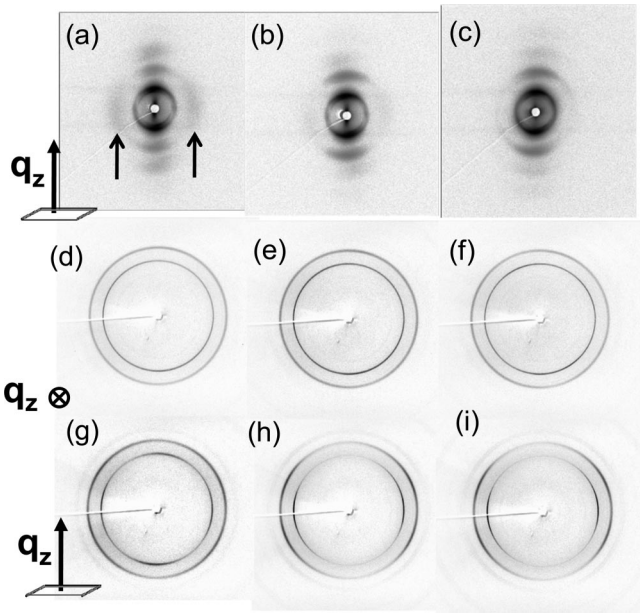

Figure 6. Set of simultaneous 2D X-ray patterns for the PS-*b*-PEO single crystal mats (26K-*b*-23K) kept at $T_{rx} = -30$ °C (a, d, g), −5 °C (b, e, h), and 30 °C (c, f, i) after melting at 64 °C for 5 min. Note that when the $T_{rx} = 30$ °C, self-seeding was utilized. 2D SAXS patterns (a, b, c) and 2D WAXS patterns (g, h, i) taken from *xy*-plane of lamellar mats and 2D WAXS patterns (d, e, f) taken from the *z*-direction of the lamellar mats. A pair of diffuse scattering arcs is located along the equator as pointed out by the arrows in (a).

density is so high that little crystal growth is needed to fill the confined space. The size of the PEO crystals generated after recrystallization is thus correspondingly small, and the PS layered confinement does not affect the PEO crystal orientation.

Figures 6a−i show a set of 2D SAXS and WAXS patterns for a PS-*b*-PEO mat (26K-*b*-23K) at different T_{rx} values between −30 and 30 °C. From the SAXS patterns along the *xy*-plane as shown in Figures 6a−c, the shape and arc positions of the patterns remain the same in the entire T_{rx} region studied. This indicates that the 1D confinement is preserved after recrystallization of the PEO blocks. In addition, Figure 6a shows a pair of diffuse diffraction arcs along the equator (labeled by arrows in this figure). This diffuse diffraction pair is attributed to the lamellar spacing of the newly crystallized PEO crystals within the confined space as previously discussed.[28]

Parts d, e, and f of Figure 6 are the 2D WAXS patterns taken from lamellar mats kept at $T_{rx} = -30$, −5, and 30 °C, respectively, when the X-ray beam is along the *z*-direction. These 2D WAXS patterns exhibit two major diffraction rings, which are identical to Figures 6b,d. These isotropic rings indicate that the PEO crystals possess a macroscopically random orientation with respect to the lamellar normal direction in this T_{rx} region. It is due to the fact that the PS-*b*-PEO single crystals were stacked with an isotropic random orientation with respect to the lamellar normal. On the other hand, Figures 6g−i are the patterns taken along the *xy*-plane of the lamellar mats. From these, two types of WAXS patterns can be found. When the sample was isothermally kept at $T_{rx} = -30$ °C for 2 h, the 2D WAXS pattern shown in Figure 6g exhibits two strong pairs of the (120) diffraction arcs along both the equator and meridian directions. The four pairs of diffraction arcs with a *d*-spacing of 0.39 nm at azimuthal angles of 35°, 65°, 115°, 145°, 215°, 245°, 295°, and 325° are the overlapped diffractions by combining two of these ($\bar{1}32$), (032), (112), ($\bar{2}12$), ($\bar{1}24$), ($\bar{2}04$), and (004) diffractions based on the role of crystallography (the azimuthal scans for both are shown in Figure 7a). This diffraction pattern can be explained by using a [$4\bar{2}1$] uniaxial

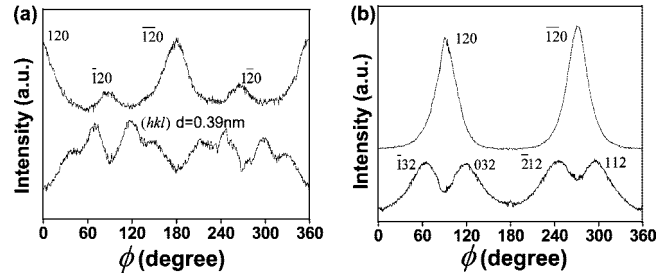

Figure 7. Azimuthal scans of Figure 6g showing the four (120) peaks (top) and overlapped diffractions of ($\bar{1}32$), (032), (112), ($\bar{2}12$), ($\bar{1}24$), ($\bar{2}04$), and (004) (bottom) (a). Azimuthal scans of Figure 6h (similar to Figure 6i) showing only one set of (120) peaks (top) and the overlapped ($\bar{2}12$) and (112) diffractions (bottom) (b).

pattern with the [$4\bar{2}1$] zone being along the meridian direction (the [$4\bar{2}1$] zone is the normal of (120) plane).[57,58] However, a mixture of the [$4\bar{2}1$] uniaxial pattern and the fiber pattern along the lamellar normal could also provide this complex 2D WAXS pattern. In order to exclude this possibility, we need to find a reflection in the fiber pattern that is not experimentally found in the [$4\bar{2}1$] uniaxial pattern.[18]

This identification can be fulfilled by analyzing the difference in the reflections on the fifth ring of the fiber pattern [the ($\bar{1}28$) and ($\bar{3}28$) planes]. The azimuthal scan angles of these two reflections with *d*-spacing of 0.21−0.22 nm are at 62°, 90°, 118°, 242°, 270°, and 298° in the predicted [$4\bar{2}1$] uniaxial pattern, but they are at 28°, 152°, 208°, and 332° in the fiber pattern. After investigating the azimuthal scan profile of the fifth ring in Figure 6g, it was found that no distinct diffraction arcs are found at azimuthal angle of 28°, 152°, 208°, and 332°. Only two weak diffraction arcs are located at azimuthal angle of 90° and 270°, and these two diffractions only appear in the [$4\bar{2}1$] uniaxial pattern. Both this finding and a pair of diffuse diffraction arcs found along the equator in the 2D SAXS pattern of Figure 6a lead to the conclusion that Figure 6g represents a pure [$4\bar{2}1$] uniaxial pattern. From this uniaxial pattern, it is deduced that the *c*-axis of PEO crystals possesses an approximately homogeneous orientation in the confined layers (the *c*-axis of the crystals is perpendicular to the lamellar normal).

The 2D WAXS patterns shown in Figures 6h,i are almost identical. In both of the patterns, only one pair of the (120) diffraction arcs is located along the equator (the azimuthal scan is shown in Figure 7b). This WAXS pattern is identical to a PEO crystal *c*-axis fiber pattern and demonstrates that the *c*-axis of the recrystallized PEO crystals is oriented approximately parallel to the lamellar normal in the mats as analyzed in our previous publications.[18,28] Note that if PEO crystals oriented perfectly parallel to the lamellar normal, then the overlapped diffractions on the second and third diffraction rings should not appear. However this 2D WAXS pattern still exhibits those diffractions (the diffractions on the third rings are weak). Based on the crystallography of PEO, the appearance of the strong overlapped ($\bar{2}12$) and (112) diffractions and the weak overlapped ($\bar{1}32$), (032), ($\bar{1}24$), ($\bar{2}04$), and (004) diffractions indicates that the deviation of the *c*-axis of the PEO crystals with respect to the lamellar normal should be between 18° and 43°, but closer to 18°. TEM ED experiments confirm that the angle of deviation from the *c*-axis is 26°.[38] This observation indicates that a PEO crystal orientation change must take place below $T_{rx} = -5$ °C, the temperature at which the *c*-axis of the recrystallized PEO crystals undergoes a transition from the homogeneous to approximately homeotropic orientation in the 1D confinement.

The PEO crystal orientation dependence on T_{rx} values in the other two diblock copolymer samples was also observed. For example, Figures 8a,b show 2D WAXS patterns of PS-*b*-PEO single crystal mats (65K-*b*-35K) with an asymmetric composi-

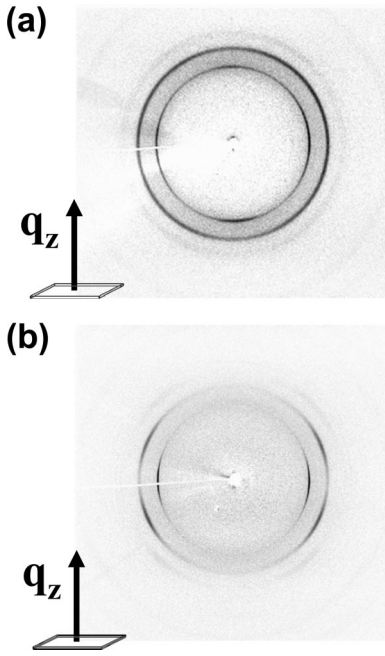

Figure 8. Two typical 2D WAXS patterns of PS-*b*-PEO single crystal mats (65K-*b*-35K) after PEO was melted at 64 °C for 5 min and kept at two different T_{rx} values for 2 h with the X-rays along the *xy*-plane. The [4$\bar{2}$1] unaxial pattern (homogeneous orientation) at $T_{rx} = -30$ °C is shown in (a), and the *c*-axis fiber pattern (homeotropic orientation) at $T_{rx} = 30$ °C is shown in (b).

tion between the two blocks (see Table 1) that were isothermally recrystallized at two T_{rx} values of −20 and 20 °C. These two figures were taken when the X-ray beam was along the *xy*-plane (see the schematic of Figure 1), and both of them exhibit two distinct *c*-axis orientations of the PEO crystals. Figure 8a represents the situation where the *c*-axis is oriented perpendicular to the lamellar normal, while Figure 8b indicates that the *c*-axis orientation is approximately parallel to the lamellar normal. Therefore, a universal trend in the *c*-axis orientation change of the recrystallized PEO crystals with T_{rx} can be identified.

However, we also observed the tilted *c*-axis orientation of the PEO crystals in bulk aligned PS-*b*-PEO samples via large amplitude mechanical shearing. This tilted orientation diminishes with an increase in the molecular weight of the blocks (equivalent to releasing the confined effect by increasing 1D confined space).[18,28] Therefore, we specifically focus on the temperature region where the *c*-axis orientation change takes place. For the PS-*b*-PEO mats (65K-*b*-35K), based on our experimental observations, the temperature region where the *c*-axis orientation changes occurs within a T_{rx} region of 5 °C. In order to examine whether the inclined *c*-axis orientation of the PEO crystals still exists within this 5 °C region or not, we specifically carried out 2D WAXD experiments of PS-*b*-PEO mats kept at $T_{rx} = -3$, −2, and −1 °C, as shown in Figures 9a−c where the X-ray beam is along the *xy*-plane. In Figure 9a, two pairs of (120) diffraction arcs located at both the equator and meridian directions indicate that the *c*-axis of the PEO crystals is perpendicular to the lamellar normal at $T_{rx} = -3$ °C, while in Figures 9b,c, the 2D WAXS patterns only possess a single pair of the (120) diffraction arcs with strong intensity along the equator direction, revealing that the *c*-axis of the recrystallized PEO crystals is parallel to the lamellar normal at $T_{rx} = -2$ and −1 °C. Note that the same recrystallization procedure in Figures 9a−c was used to obtain crystals above and below the T_{rx} values where the crystal orientation change occurs (perpendicular and approximately parallel to the lamellar normal). Therefore, it can be concluded that a sharp change of the PEO crystal orientation from perpendicular to approximately

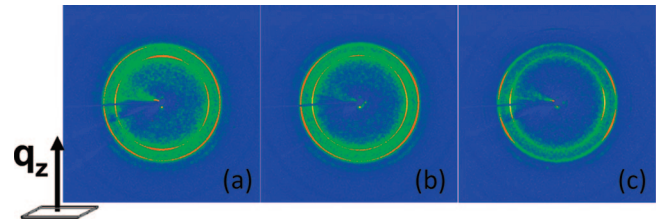

Figure 9. Set of 2D WAXS patterns of PS-*b*-PEO single crystal mats (65K-*b*-35K) kept at $T_{rx} = -3$ °C (a), $T_{rx} = -2$ °C (b), and $T_{rx} = -1$ °C (c) for 2 h after the PEO crystals were melted at 64 °C for 5 min. The X-ray beam is along the *xy*-plane.

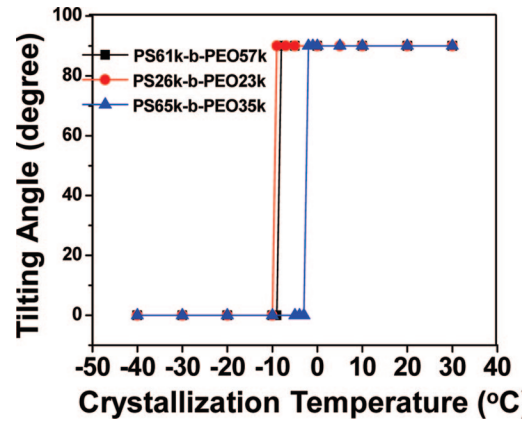

Figure 10. Similarities in transition temperature region between T_{rx}-dependent crystal orientation changes for three different PS-*b*-PEO lamellar mats.

parallel with respect to the lamellar normal takes place within 1 °C. No tilted orientation can be observed in this set of single crystal mats. It is speculated that the tilted *c*-axis orientation results from the sample preparation of large amplitude mechanical shearing. Further investigation is required.

Figure 10 presents a summary of the *c*-axis orientation changes for three PS-*b*-PEO diblock copolymer mats. Two crystal orientations, namely, the *c*-axis of the recrystallized PEO crystals perpendicular and approximately parallel to the lamellar normal, exist in the T_{rx} region studied. In addition, when these three mats were quenched to liquid N_2 from the PEO melt, random *c*-axis orientation is found between two glassy PS confined layers. This finding confirms that these two types of crystal orientation should originate from the metastable states with local free energy minima affected by the 1D confined lamellar environment.[49] It is also interesting that the temperatures at which the orientation change occurs are different. Apparently, the PS-*b*-PEO mat having an asymmetric block composition (65K-*b*-35K) exhibits a higher temperature of −3 °C, compared with two other mats having relatively symmetric block compositions (−10 °C).

Origin of the Crystal Orientation Change. In order to explain the sharp crystal orientation change within a narrow T_{rx} as shown in Figure 10, we need to carefully examine the "sandwiched"-type confined template. As described in our previous publication, PEO block recrystallization does not take place until T_{rx} is lower than −5 °C.[38] This experimental observation is also supported by our DSC results shown in Figure 4. The results indicate that after growing single crystals in dilute solution no heterogeneous nucleation sites (foreign particles) in these single crystals are possible.[38] The only possible heterogeneous nucleation event in our single-crystal system is via self-seeding.[40−44] Therefore, homogeneous nucleation dominates the PEO recrystallization at high supercooling

while the recrystallization of PEO at low supercooling can only be achieved via self-seeding in the confined lamellae.

It is known that the onset temperature of homogeneous nucleation of PEO bulk samples is between −10 and 0 °C, as a weak function of the PEO molecular weight.[59,60] Furthermore, the onset temperature of homogeneous nucleation is affected by confined volume as identified[59] and summarized in the case of droplets (spheres).[29] For example, a T_x value of −40 °C was found in isolated PEO spheres with a diameter of 10 nm in PEO diblock copolymer,[61,62] which is significantly lower than that in the PEO droplet experiments with a volume ranging from 10 to 1000 μm^3.[29,59,61−63] In our study, we have observed that the T_{rx} values where the sharp change of the crystal orientation takes place is between −10 and −3 °C. Does this sharp change also correspond to the onset temperature of homogeneous nucleation as observed in PEO homopolymers evaluated utilizing the droplet experiments on the μm^3 scale?

In order to answer this question, let us analyze the confined volume dependence of the onset temperature of homogeneous nucleation. In our system, the confined volume of the PS-*b*-PEO single crystal mats is 16 μm^3 (40 × 40 × 0.01 μm^3), which is on the same order as that of the PEO droplet experiment. If we do not consider the geometric shape, but only the volume effect on the onset temperature of homogeneous nucleation, both cases should exhibit similar crystallization behavior. However, we speculate that the geometric shape might also affect this onset temperature. A systematic study is currently being carried out and will be reported in the future. At this moment, we can only state that our observation of the onset temperature of the sharp orientation change of the PEO crystals may only be coincidently correlated with the onset temperature of homogeneous nucleation.

Now, what is the mechanism to cause the *c*-axis orientation change in the PEO crystals? Macroscopically, a thermodynamic consideration requires that the overall crystallinity of the recrystallized PEO crystals must reach the maximum, while kinetics demands that the PEO recrystallization lead to a maximum crystallinity in the shortest time.[49] Microscopically, several molecular factors affecting the *c*-axis orientation in the PEO crystals may be considered. First, the junction between the PS and PEO blocks is expected to affect the PEO segmental conformations near the interface, and they may have a preferred orientation parallel to the lamellar normal due to a microphase separation driving force. This type of orientation should also depend upon the tethering density, σ.[41−43] A higher σ value may promote preferential segmental orientation toward the lamellar normal direction and thus will influence the crystal orientation. Both factors may help the *c*-axis of the PEO crystals to be oriented approximately parallel to the lamellar normal. Such an effect has been examined theoretically by Monte Carlo simulation experiments.[64] On the other hand, the higher M_n^{PS} and M_n^{PEO} may lead to disassociations of the PEO blocks with their junction points and encourage a deviation of this orientation.[64] Note that only when the *c*-axis of the PEO crystals is parallel to the lamellar normal can both sets of the (120) planes grow laterally along the direction perpendicular to the lamellar normal. Therefore, this is a 2D growth to ensure the development of maximum crystallinity.

Second, the density fluctuations of the PEO melt before the crystallization also become anisotropic along both the perpendicular and parallel directions due to the existence of the 1D confinement. From the viewpoint of critical nucleus formation, since the ability to overcome the nucleation barrier relies on the density fluctuation, in this case, it becomes different for these two directions. Furthermore, the confined space (the thickness of the PEO single crystal) is on the same order of magnitude as the radius of gyration of the PEO blocks (here, the R_g^{PEO} of he

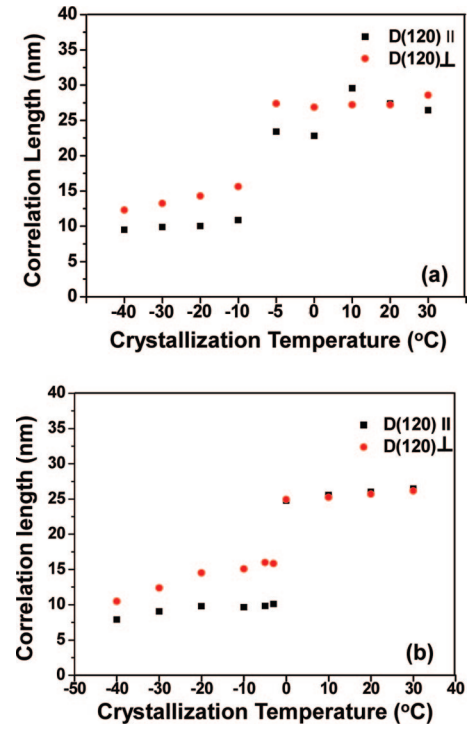

Figure 11. Apparent crystal sizes (correlation lengths) for the two pairs of (120) reflections in the 2D WAXS patterns along both the *xy*-plane and *z*-direction with respect to different T_{rx} values for PS-*b*-PEO (26K-*b*-23K) (a) and PS-*b*-PEO (65K-*b*-35K) mats (b).

three PS-*b*-PEO samples in the bulk is between 5.83 and 9.16 nm). The distances between two PS layers in this study are ∼10 nm along the lamellar normal; therefore, the confined space is smaller than $2R_g^{PEO}$. Under these conditions, the overall chain conformation becomes anisotropic in the melt, which may affect the *c*-axis orientation of the PEO crystals. Both the anisotropies of the overall chain conformation and the density fluctuation of the melt in the 1D confinement of ∼10 nm favor the *c*-axis orientation of the PEO crystals perpendicular to the lamellar normal. This leads to the case that only one set of (120) planes can grow, and it is thus a 1D crystal growth. This homogeneous nucleation mechanism has been recently examined theoretically by linearized time-dependent Ginzburg−Landau equations.[65] On the basis of these analyses, we can deduce that the experimentally observed *c*-axis orientations of the PEO crystals perpendicular and approximately parallel to the lamellar normal at different T_{rx} values must be a result of competition among these factors. However, detailed effects of these factors on the orientation change in the PEO crystals are still forthcoming.

The change of the *c*-axis orientation, and thus the change from the 1D to 2D growth with increasing T_{rx} values in the recrystallized PEO crystals, can also be illustrated by calculating the crystallite size using the Sherrer equation with the WAXS patterns. Parts a and b of Figure 11 show the trend between the change in crystallite sizes of the two orthogonal (120) planes' normal directions (or growth directions) ($D_{120,\parallel}$ and $D_{120,\perp}$) with respect to T_{rx} values for two different PS-*b*-PEO mats, (65K-*b*-35K) and (26K-*b*-23K), respectively. The $D_{120,\parallel}$ and $D_{120,\perp}$ represent the correlation lengths of the (120) plane normal directions parallel and perpendicular to the lamellar normal. In the region of −40 °C ≤ T_{rx} ≤ −10 °C in both cases, the crystal growth is 1D, and one set of the (120) growth planes ($D_{120,\parallel}$) are confined by two nano-PS layers. Their crystallite sizes are thus limited by the PEO layer thicknesses of around 10 nm. Another set of the (120) growth planes ($D_{120,\perp}$) can be larger than this limit since their growth is only stopped by the impingement with the neighboring crystals. The slight increase

of the $D_{120,\perp}$ values in both figures represents decreases of the homogeneous nucleation density with increasing T_{rx} values. However, when T_{rx} exceeds the onset temperature of the orientation change of the PEO crystals, such as $T_{rx} = -7$ °C for PS-*b*-PEO (26K-*b*-23K) mats, both the $D_{120,\parallel}$ and $D_{120,\perp}$ values exhibit sudden increases, and their sizes now become almost identical. This indicates a 2D crystal growth. Note that in this T_{rx} region the crystallite sizes may not represent the true crystal sizes; rather, they are the average correlation lengths along the normal of the (120) planes within the recrystallized crystals.

Since three PS-*b*-PEO single crystal mats with different molecular weights and compositions are grown at the same crystallization temperature in dilute solution, the samples have almost identical confined size and reduced tethering density. In order to further verify the discussed mechanism of the *c*-axis orientation change in the PEO crystals described above and the roles of these two factors separately on the crystal orientation change, we would like to have a series of single crystal mats which possess an identical 1D confinement size with different reduced tethering densities and another series of single crystal mats with different 1D confined spaces yet having similar reduced tethering densities. By investigating the onset temperature of the *c*-axis orientation change for those PS-*b*-PEO single crystal mats, we can achieve further understanding of these competing factors.

Conclusion

In summary, an extended approach has been proposed to utilize stacked mats of the "sandwiched" lamellar single crystals of three PS-*b*-PEO block copolymers grown in dilute solution to investigate the PEO crystal orientation change with respect to the confined lamellar geometry at different T_{rx} values. These PS-*b*-PEO single crystal mats exhibit excellent lamellar orientation along the lamellar normal direction as evidenced by 2D SAXS experiments. Since the glass transition temperature of the nano-PS layers is higher than the melting temperature of the PEO single crystals in the PS-*b*-PEO mats, the melting and recrystallization process of the PEO blocks is in a hard-confined environment constructed by two glassy PS nanolayers. The 2D WAXS results show that the PEO crystal orientation is T_{rx} dependent. With an increase in the T_{rx}, the PEO crystals adopt a random orientation at deep supercooling, an orientation with the *c*-axis of the crystals perpendicular to the lamellar normal (homogeneous), and finally an orientation with the *c*-axis approximately parallel to the lamellar normal (homeotropic). A sharp change of PEO crystal orientation from perpendicular to parallel occurs within 1 °C of the temperature, which is coincident with the onset temperature of homogeneous nucleation. The crystal orientation change has been achieved by the compromise between the thermodynamics of reaching the maximum crystallinity and the kinetics of the fastest crystallization direction. Microscopically, the mechanism of this change may have resulted from a competition of the PEO segmental orientation near the PS and PEO interfaces which is determined by tethering density with anisotropies of the overall chain conformation and density fluctuation of the PEO melt due to the confinement of the PS layers. This study hopes to provide a possible reason to understand the long-standing issue of the origin of crystal orientation changes in 1D confined crystallization. Further investigation of the effects of confined geometric shape and tethering density is currently ongoing.

Acknowledgment. This work was supported by NSF (DMR-0516602). The 2D SAXS and WAXS search was partially carried out at the National Synchrotron Light Source in Brookhaven National Laboratory supported by the Department of Energy (DOE).

References and Notes

(1) Hamley, I. W. *The Physics of Block Copolymers*; Oxford University Press: New York, 1998.
(2) Cohen, R. E.; Cheng, P. L.; Douzinas, K. C.; Kofinas, P.; Berney, C. V. *Macromolecules* **1990**, *23*, 324.
(3) Douzinas, K. C.; Cohen, R. E. *Macromolecules* **1992**, *25*, 5030.
(4) Sakurai, K.; MacKnight, W. J.; Lohse, D. J.; Schulz, D. N.; Sissano, J. A. *Macromolecules* **1993**, *26*, 3236.
(5) Cohen, R. E.; Bellare, A.; Drzewinski, M. A. *Macromolecules* **1994**, *27*, 2321.
(6) Khandpur, A. K.; Macosko, C. W.; Bates, F. S. *J. Polym. Sci., Polym. Phys. Ed.* **1995**, *33*, 2.
(7) Hamley, I. W.; Fairclough, J. P. A.; Ryan, A. J.; Bates, F. S.; Towns-Andrews, E. *Polymer* **1996**, *37*, 4425.
(8) Zhao, J.; Majumdar, B.; Schulz, M. F.; Bates, F. S.; Almdal, K.; Mortensen, K.; Hajduk, D. A.; Gruner, S. M. *Macromolecules* **1996**, *29*, 1204.
(9) Liu, L. Z.; Yeh, F.; Chu, B. *Macromolecules* **1996**, *29*, 5336.
(10) Hamley, I. W.; Fairclough, J. P. A.; Terrill, N. J.; Ryan, A. J.; Lipic, P. M.; Bates, F. S.; Towns-Andrews, E. *Macromolecules* **1996**, *29*, 8835.
(11) Quiram, D. J.; Register, R. A.; Marchand, G. R. *Macromolecules* **1997**, *30*, 4551.
(12) Quiram, D. J.; Register, R. A.; Marchand, G. R.; Ryan, A. J. *Macromolecules* **1997**, *30*, 8338.
(13) Quiram, D. J.; Register, R. A.; Marchand, G. R.; Adamson, D. H. *Macromolecules* **1998**, *31*, 4891.
(14) Zhu, L.; Chen, Y.; Zhang, A.; Calhoun, B. H.; Chun, M.; Quirk, R. P.; Cheng, S. Z. D.; Hsiao, B. S.; Yeh, F.; Hashimoto, T. *Phys. Rev. B* **1999**, *60*, 10022.
(15) Park, C.; De Rosa, C.; Fetters, L. J.; Thomas, E. L. *Macromolecules* **2000**, *33*, 7931.
(16) Loo, Y. L.; Register, R. A.; Ryan, A. J. *Phys. Rev. Lett.* **2000**, *84*, 4120.
(17) Loo, Y. L.; Register, R. A.; Adamson, D. H. *Macromolecules* **2000**, *33*, 8361.
(18) Zhu, L.; Cheng, S. Z. D.; Calhoun, B. H.; Ge, Q.; Quirk, R. P.; Thomas, E. L.; Hsiao, B. S.; Yeh, F.; Lotz, B. *J. Am. Chem. Soc.* **2000**, *122*, 5957.
(19) Zhu, L.; Calhoun, B. H.; Chun, M.; Quirk, R. P.; Cheng, S. Z. D.; Thomas, E. L.; Lotz, B.; Hsiao, B. S.; Yeh, F.; Liu, L. *Macromolecules* **2001**, *34*, 1244.
(20) Huang, P.; Zhu, L.; Cheng, S. Z. D.; Ge, Q.; Quirk, R. P.; Thomas, E. L.; Lotz, B.; Hsiao, B. S.; Liu, L.; Yeh, F. *Macromolecules* **2001**, *34*, 6649.
(21) Zhu, L.; Cheng, S. Z. D.; Huang, P.; Ge, Q.; Quirk, R. P.; Thomas, E. L.; Lotz, B.; Hsiao, B. S.; Yeh, F.; Liu, L. *Adv. Mater.* **2002**, *14*, 31.
(22) Zhu, L.; Huang, P.; Chen, W. Y.; Ge, Q.; Quirk, R. P.; Cheng, S. Z. D.; Thomas, E. L.; Lotz, B.; Hsiao, B. S.; Yeh, F.; Liu, L. *Macromolecules* **2002**, *35*, 3553.
(23) Loo, Y. L.; Register, R. A.; Ryan, A. J. *Macromolecules* **2002**, *35*, 2365.
(24) Xu, J.-T.; Fairclough, J. P. A.; Mai, S.-M.; Ryan, A. J.; Chaibundit, C. *Macromolecules* **2002**, *35*, 6937.
(25) Xu, J.-T.; Fairclough, J. P. A.; Mai, S.-M.; Chaibundit, C.; Mingvanish, M.; Booth, C.; Ryan, A. J. *Polymer* **2003**, *44*, 6843.
(26) Reiter, G.; Castelein, G.; Sommer, J.-U. In *Polymer Crystallization: Observations, Concepts and Interpretations*; Sommer, J.-U., Reiter, G., Eds.; Springer: Berlin, 2003; Chapter 8.
(27) Loo, Y.-L.; Register, R. A. In *Developments in Block Copolymer Science and Technology*; Hamley, I. W., Ed.; Wiley: New York, 2004; Chapter 6.
(28) Huang, P.; Zhu, L.; Guo, Y.; Ge, Q.; Jing, A. J.; Chen, W. Y.; Quirk, R. P.; Cheng, S. Z.; D, Thomas, E. L.; Lotz, B.; Hsiao, B. S.; Avila-Orta, C. A.; Sics, I. *Macromolecules* **2004**, *37*, 3689.
(29) Müller, A. J.; Balsamo, V.; Arnal, M. L. *Adv. Polym. Sci.* **2005**, *190*, 1.
(30) Huang, P.; Guo, Y.; Quirk, R. P.; Ruan, J.; Lotz, B.; Thomas, E. L.; Hsiao, B. S.; Avila-Orta, C. A.; Sics, I.; Cheng, S. Z. D. *Polymer* **2006**, *47*, 5457.
(31) Sun, Y. S.; Chung, T. M.; Li, Y. J.; Ho, R. M.; Ko, B. T.; Jeng, U. S.; Lotz, B. *Macromolecules* **2006**, *39*, 5782.
(32) Huang, P.; Zheng, J. X.; Leng, S.; Van Horn, R. M.; Jeong, K. U.; Guo, Y.; Quirk, R. P.; Cheng, S. Z. D.; Lotz, B.; Thomas, E. L.; Hsiao, B. S. *Macromolecules* **2007**, *40*, 526.
(33) Sun, Y. S.; Chung, T. M.; Li, Y. J.; Ho, R. M.; Ko, B. T.; Jeng, U. S.; Lotz, B. *Macromolecules* **2007**, *40*, 6781.
(34) Wunderlich, B. *Macromolecular Physics*; **1973**; Vol. *I*, Chapter 4.
(35) Gido, S. P.; Thomas, E. L. *Macromolecules* **1994**, *27*, 6137.
(36) Marencic, A. P.; Wu, M. W.; Register, R. A.; Chaikin, P. M. *Macromolecules* **2007**, *40*, 7299.

(37) Zhu, L.; Cheng, S. Z. D.; Calhoun, B. H.; Ge, Q.; Quirk, R. P.; Thomas, E. L.; Hsiao, B. S.; Yeh, F.; Lotz, B. *Polymer* **2001**, *42*, 5829.
(38) Hsiao, M.-S.; Chen, W. Y.; Zheng, J. X.; Van Horn, R. M.; Quirk, R. P.; Ivanov, D. A.; Thomas, E. L.; Lotz, B.; Cheng, S. Z. D. *Macromolecules* **2008**, *41*, 4794.
(39) Quirk, R. P.; Kim, J.; Kausch, C.; Chun, M. S. *Polym. Int.* **1996**, *39*, 3.
(40) Lotz, B.; Kovacs, A. J.; Bassett, G. A.; Keller, A. *Kolloid Z. Z. Polym.* **1966**, *209*, 115.
(41) Chen, W. Y.; Zheng, J. X.; Cheng, S. Z. D.; Li, C. Y.; Huang, P.; Zhu, L.; Xiong, H.; Ge, Q.; Guo, Y.; Quirk, R. P.; Lotz, B.; Deng, L.; Wu, C.; Thomas, E. L. *Phys. Rev. Lett.* **2004**, *93*, 028301.
(42) Chen, W. Y.; Li, C. Y.; Zheng, J. X.; Huang, P.; Zhu, L.; Ge, Q.; Quirk, R. P.; Lotz, B.; Deng, L.; Wu, C.; Thomas, E. L.; Cheng, S. Z. D. *Macromolecules* **2004**, *37*, 5292.
(43) Zheng, J. X.; Xiong, H.; Chen, W. Y.; Lee, K.; Van Horn, R. M.; Quirk, R. P.; Lotz, B.; Thomas, E. L.; Shi, A.-C.; Cheng, S. Z. D. *Macromolecules* **2006**, *39*, 641.
(44) Lotz, B.; Kovacs, A. J. *Kolloid Z. Z. Polym.* **1966**, *209*, 97.
(45) Organ, S. J.; Keller, A. *J. Mater. Sci.* **1985**, *20*, 1571.
(46) Organ, S. J.; Keller, A. *J. Mater. Sci.* **1985**, *20*, 1602.
(47) Cheng, S. Z. D.; Wunderlich, B. *J. Polym. Sci., Polym. Phys. Ed.* **1986**, *24*, 577.
(48) Alexander, L. E. *X-ray Diffraction Methods in Polymer Science*; Wiley-Interscience: New York, 1969.
(49) Cheng, S. Z. D. *Phase Transitions in Polymers, the Role of Metastable States*; Elsevier: Amsterdam, 2008.
(50) Ellison, C. J.; Mundra, M. K.; Torkelson, J. M. *Macromolecules* **2005**, *38*, 1767.
(51) Alcoutlabi, M.; McKenna, G. B. *J. Phys.: Condens. Matter* **2005**, 17R461.
(52) Park, J.-Y.; McKenna, G. B. *Phys. Rev. B* **2000**, *61*, 6667.
(53) Arnold, F. E., Jr.; Cheng, S. Z. D.; Hsu, S. L.-C.; Lee, C. J.; Harris, F. W. *Polymer* **1992**, *24*, 5179.
(54) Arnold, F. E., Jr.; Shen, D.; Lee, C. J.; Harris, F. W.; Cheng, S. Z. D.; Starkweather, H. W., Jr. *J. Mater. Chem.* **1993**, *3*, 183.
(55) Arnold, F. E., Jr.; Shen, D.; Lee, C. J.; Harris, F. W.; Cheng, S. Z. D.; Lau, S.-F. *J. Mater. Chem.* **1993**, *3*, 353.
(56) Castillo, R. V.; Arnal, M. L.; Müller, A. J.; Hamley, I. W.; Castelletto, V.; Schmalz, H.; Abetz, V. *Macromolecules* **2008**, *41*, 879.
(57) Takahashi, Y.; Tadokoro, H. *Macromolecules* **1973**, *6*, 672.
(58) Tadokoro, H.; Chatani, Y.; Yoshihara, T.; Tahara, S.; Murahashi, S. *Makromol. Chem.* **1964**, *73*, 109.
(59) Massa, M. V.; Dalnoki-Veress, K. *Phys. Rev. Lett.* **2004**, *92*, 255509.
(60) Koutsky, J. A.; Walton, A. G.; Baer, E. *J. Appl. Phys.* **1967**, *38*, 1832.
(61) Chen, H. L.; Hsiao, S. C.; Lin, T. L.; Yamauchi, K.; Hasegawa, H.; Hashimoto, T. *Macromolecules* **2001**, *34*, 671.
(62) Müller, A. J.; Balsamo, V. M.; Arnal, L.; Jakob, T.; Schmalz, H.; Abetz, V. *Macromolecules* **2002**, *35*, 3048.
(63) Massa, M. V.; Carvalho, J. L.; Dalnoki-veress, K. *Eur. Phys. J. E* **2003**, *12*, 111.
(64) Hu, W.; Frenkel, D. *Faraday Discuss.* **2005**, *128*, 253.
(65) Tan, H.; Miao, B.; Yan, D. *J. Chem. Phys.* **2003**, *119*, 2886.

MA801641W